Geoscience Frontiers 11 (2020) 1669–1680

Contents lists available at ScienceDirect

Geoscience Frontiers

journal homepage: www.elsevier.com/locate/gsf

Research Paper

East African topography and volcanism explained by a single, migrating plume

Rakib Hassan [a,c,*], Simon E. Williams [a,d], Michael Gurnis [b], Dietmar Müller [a]

[a] School of Geosciences, Room 412, Madsen Building F09 Eastern Avenue, The University of Sydney, NSW, 2006, Australia
[b] Seismological Laboratory, California Institute of Technology, Pasadena, CA, 91125, USA
[c] Now at Geoscience Australia, GPO Box 378, Canberra, ACT, 2601, Australia
[d] State Key Laboratory of Continental Dynamics, Department of Geology, Northwest University, Xi'an 710069, China

ARTICLE INFO

Handling Editor: Richard M Palin

Keywords:
Numerical mantle flow models
Deep mantle flow
LLSVP morphology
Plume dynamics
Plume motion
Dynamic topography

ABSTRACT

Anomalous topographic swells and Cenozoic volcanism in east Africa have been associated with mantle plumes. Several models involving one or more fixed plumes beneath the northeastward migrating African plate have been suggested to explain the space-time distribution of magmatism in east Africa. We devise paleogeographically constrained global models of mantle convection and, based on the evolution of flow in the deepest lower mantle, show that the Afar plume migrated southward throughout its lifetime. The models suggest that the mobile Afar plume provides a dynamically consistent explanation for the spatial extent of the southward propagation of the east African rift system (EARS), which is difficult to explain by the northeastward migration of Africa over one or more fixed plumes alone, over the last ≈45 Myr. We further show that the age-progression of volcanism associated with the southward propagation of EARS is consistent with the apparent surface hotspot motion that results from southward motion of the modelled Afar plume beneath the northeastward migrating African plate. The models suggest that the Afar plume became weaker as it migrated southwards, consistent with trends observed in the geochemical record.

1. Introduction

The long-wavelength topographic structure associated with the high Ethiopian plateau, along with the contiguous eastern and southern African plateaus is known as the African superswell (Nyblade and Robinson, 1994). Anomalous topographic swells in east Africa are associated with Tertiary flood basalt eruptions and magmatism stretching from northwestern Ethiopia to northern Tanzania (Fig. 1). The anomalous topography of southern Africa, on the other hand, is thought to be sustained by the large low shear velocity province (LLSVP) and the associated large-scale mantle upwelling under southern Africa (Lithgow-Bertelloni and Silver, 1998; Gurnis et al., 2000). Recently, isostatic uplift resulting from plume-triggered lithospheric delamination has also been suggested to explain a fraction of the anomalous topography in the region (Hu et al., 2018).

The largest eruptions occur on the Ethiopian and east African plateaus, which are both transected by the east African rift system (Fig. 1b). The oldest eruptions associated with EARS occurred between 45 Ma and 35 Ma and volcanism systematically progressed southward from southern Ethiopia to Tanzania (George et al., 1998). The absence of significant rifting synchronous with earliest volcanism (Pik et al., 2008) and the generally small degrees of extension observed (Burke, 1996) suggest that one or more plumes may have impinged beneath the plateaus. Furthermore, geochemical studies (George et al., 1998; Nelson et al., 2008) and inferences from the gravity field (Ebinger et al., 1989) provide further evidence for plume-related doming.

The uplift history of east Africa has influenced paleodrainage systems and has major implications for paleoclimatic variations that influenced the evolution of life regionally. Formation of EARS and associated regional uplift influenced major river systems including the Congo, Nile and Zambezi rivers (Pik et al., 2003; Goudie, 2005; Stankiewicz and de Wit, 2005; Underwood et al., 2013). Stankiewicz and de Wit (2005) suggested that the Congo basin drained into the Indian Ocean prior to the formation of EARS — consequently, the Congo basin became landlocked. Subsequently, river capture events in the Miocene linked the Congo basin to the Atlantic (Goudie, 2005; Stankiewicz and de Wit, 2005).

* Corresponding author. School of Geosciences, Room 412, Madsen Building F09 Eastern Avenue, The University of Sydney, NSW, 2006, Australia.
E-mail address: rakib.hassan@ga.gov.au (R. Hassan).
Peer-review under responsibility of China University of Geosciences (Beijing).

https://doi.org/10.1016/j.gsf.2020.01.003
Received 29 January 2019; Received in revised form 27 October 2019; Accepted 1 January 2020
Available online 20 January 2020

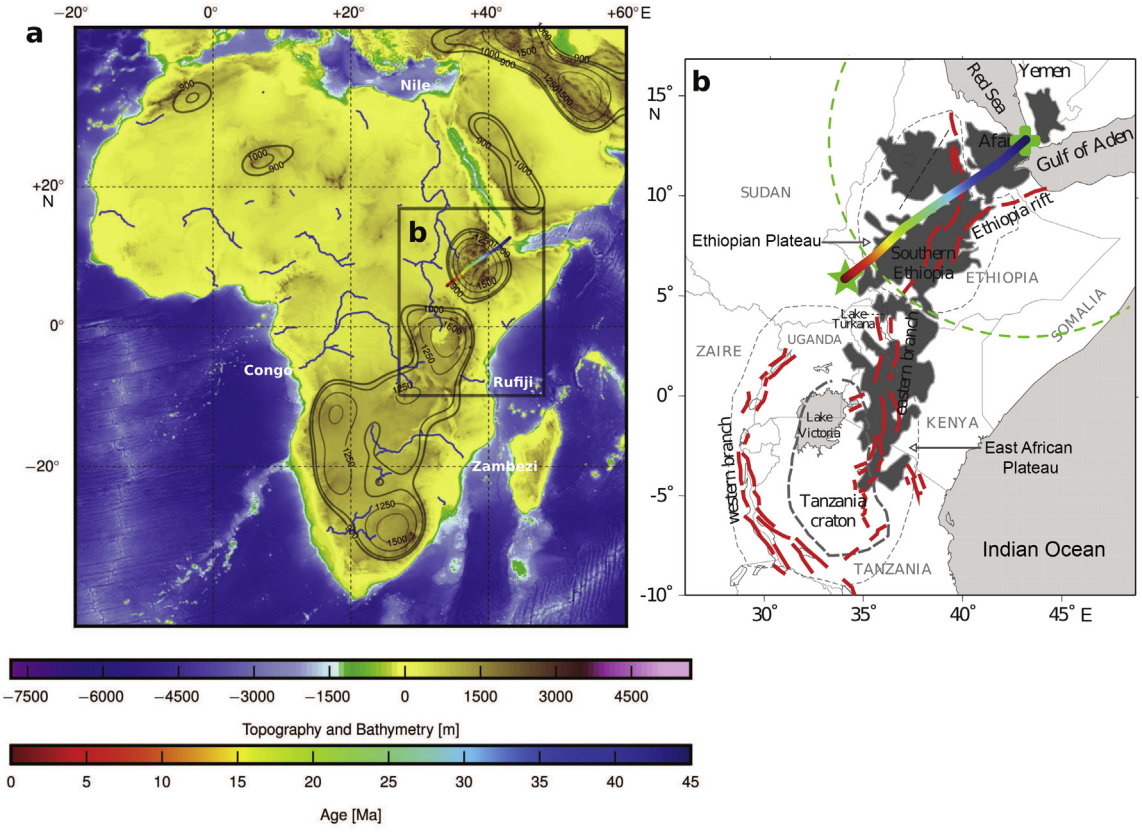

Fig. 1. African superswell and the east African rift system. (a) Elevation map of Africa (Amante and Eakins, 2009), along with major drainage systems (Strahler number ≥ 7 (Stankiewicz and de Wit, 2005)). Long-wavelength contours, showing the spherical harmonic expansion of Earth's topography up to 40°, highlight the extent of the superswell. The multicolored line shows the trajectory traced by a fixed Afar plume on the African plate as it moved northeastward over the last 45 Myr. (b) A map of eastern Africa (figure redrawn after Lin et al. (2005)) showing the distribution of Tertiary basalts (in dark grey), the east African rift system (in red dashed lines) and the Ethiopian and east African plateaus (in thin grey dashed lines). The dashed circle in green marks a plume head with a radius of 1000 km, with its center marked by the cross symbol in green. The plume is assumed to have erupted at 34°E, 6°N (marked by the star symbol in green), see Ebinger and Sleep (1998) and Steinberger (2000) for further details.

Table 1
Physical parameters and constants.

Parameter	Symbol	Value	Units
Rayleigh number	Ra	5×10^8	–
Earth radius	R_0	6371	km
Density	ρ_0	3930	kg m^{-3}
Thermal expansivity	α_0	1.42×10^{-5}	K^{-1}
Thermal diffusivity	κ_0	1×10^{-6}	m^2 s^{-1}
Specific heat capacity	C_p	1100	J kg^{-1} K^{-1}
Gravitational acceleration	g	10	m s^{-2}
Surface Temperature	T_s	300	K
Dissipation number	Di	0.8	–
Reference Viscosity	η_0	1×10^{21}	Pa s
Internal Heating	H	100	–

Table 2
Model-specific input and output parameters.

Case	Input parameters				Output parameters
	$\Delta\rho_{ch}$ (%)	APM model	Δd (km)	Geometry of dense layer	Age of Afar eruption (Ma)
M1	3.5	APM1	100	Uniform	100
M2[a]	3.0	APM1	100	Uniform	90
M3	2.5	APM2	150	Uniform	100
M4	3.0	APM2	150	Uniform	75
M5	3.5	APM2	100	Uniform	115
M6	2.5	APM2	–	Domed	75

Δd and $\Delta\rho_{ch}$ are the thickness of the dense thermochemical layer and its anomalous chemical density as a percentage, respectively.
[a] Preferred model, see section 4.

A large Afar plume head eruption beneath Ethiopia has been suggested to explain the Cenozoic magmatism throughout east Africa (Ebinger and Sleep, 1998). However, whether a single plume can account for widespread volcanism observed regionally has been questioned. Although volcanism had started at 45 Ma in southern Ethiopia, magmatism reached a peak in northern Ethiopia at ~30 Ma (George et al., 1998; Rooney, 2017), and geochemical studies indicate what has been interpreted as the presence of two distinct plume sources (George et al., 1998; Rogers, 2006; Nelson et al., 2008). In addition, a model involving three separate plumes has also been proposed (Burke, 1996).

Numerical models aimed at better understanding EARS and its interaction with one or more plumes have so far been limited in scope. In particular, numerical models with fully dynamic plumes evolving in global flow fields, constrained by paleogeography, have thus far not been employed to study the evolution of EARS. Ebinger and Sleep (1998) assumed a fixed Afar plume from 45 Ma, below a slow moving African plate. The hotspot track created by a fixed Afar plume on the African plate (Fig. 1b) and an initial plume head radius of ~1000 km (Fig. 1b) suggest that the eastern and western branches of EARS are beyond the reach of magma erupted from a single, stationary plume — consequently, their study did not include the propagation of plume material beneath the western and eastern branches of the rift system under present-day Tanzania (Fig. 1b). Furthermore, the fixed-plume scenario requires

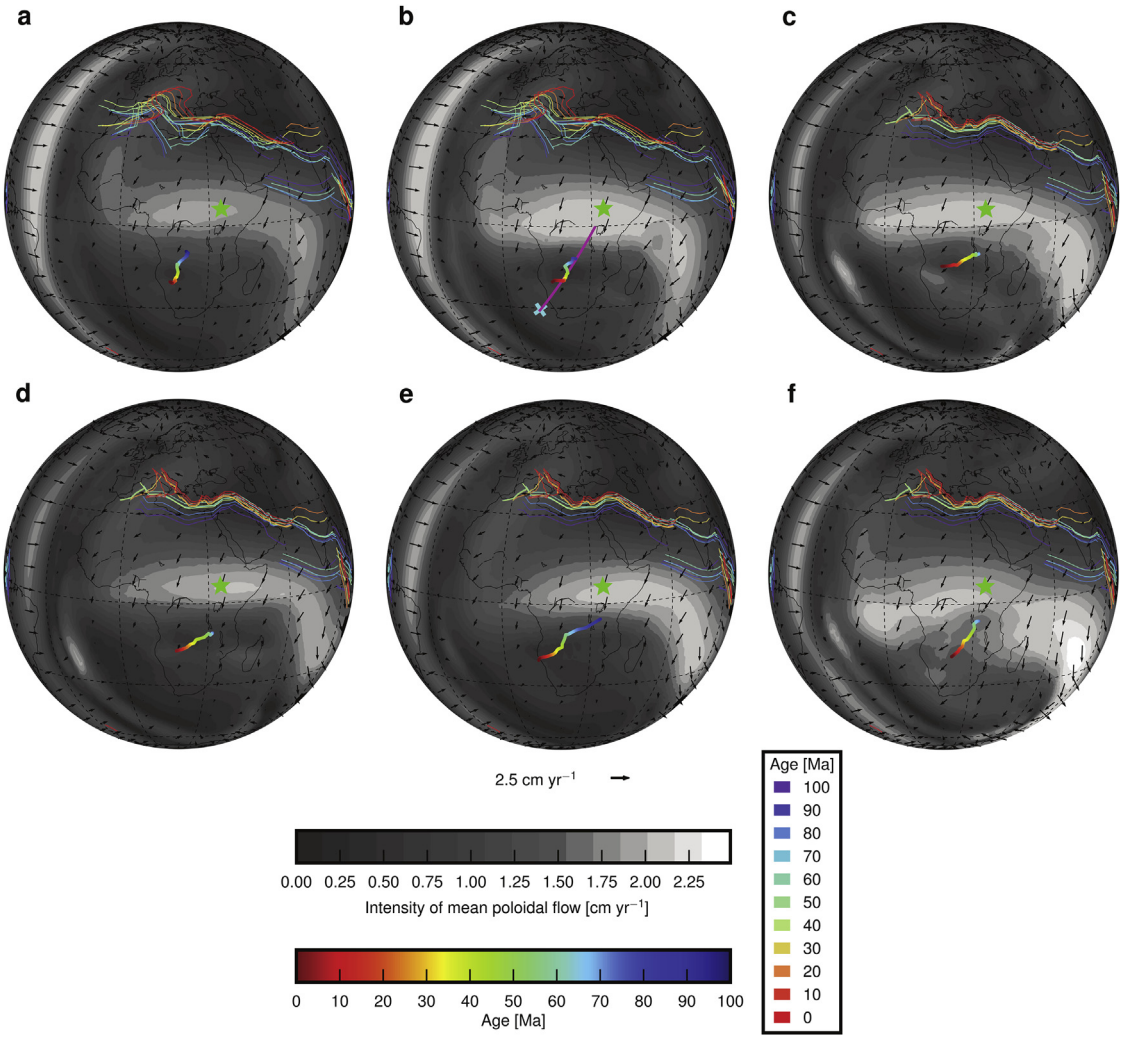

Fig. 2. A comparison of flow analytics in the deepest lower mantle. (a) In model M1, the time-averaged mean poloidal flow in the deepest lower mantle (see text) over the last 100 Myr is shown in the background and associated velocity vectors are shown in the foreground. Subduction zones over the last 100 Myr are shown at 10 Myr intervals. The multicolored trajectory shows the location of model Afar plume in mantle frame of reference (at a depth of 350 km) through time since eruption. The star symbol in green is as described in Fig. 1b. Present-day coastlines are shown in black. (b–f) The same as in (a), but for models M2, M3, M4, M5 and M6, respectively.

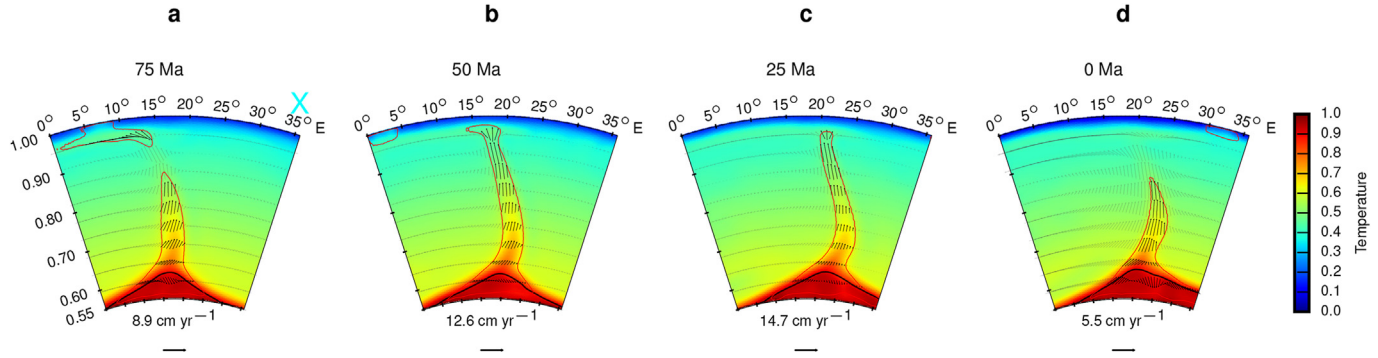

Fig. 3. Southward motion of the model Afar plume. Cross-section through model M2 (magenta profile in Fig. 2b), at (a) 75 Ma, (b) 50 Ma, (c) 25 Ma and (d) 0 Ma, showing the nondimensional temperature field, flow velocities and the conduit of the model Afar plume anchored to the LLSVP. Temperature away from layer averages in the panel is contoured by the depth-averaged standard deviation of layer temperature values to delineate the plume conduit in red. The thick black contour marks 75% anomalous chemical concentration. Velocity vectors outside of the plume conduit are shown in grey to avoid visual clutter. Note that since the plume trajectory and the magenta profile (Fig. 2b) does not coincide at all times over the last 75 Ma, the entire plume conduit that extends from the CMB to the surface could not be captured in all the panels shown here.

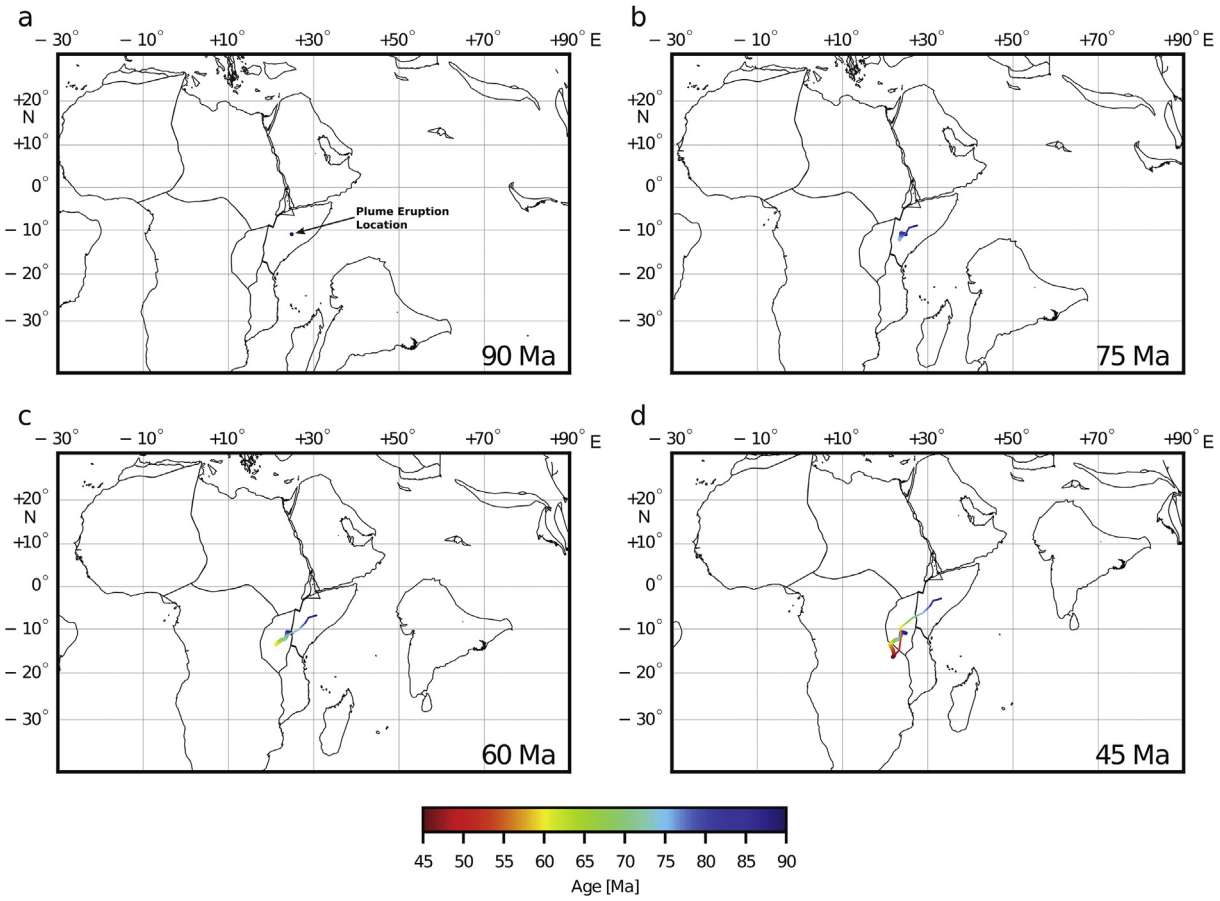

Fig. 4. Lateral motion of the model Afar plume. (a) Model Afar plume eruption location in model M2 and coastlines at 90 Ma, reconstructed based on APM1. (b–d) The thicker, multicolored trajectory in each panel shows the motion of the model Afar plume in model M2 in the mantle frame of reference, up to the labelled age since erupting at 90 Ma. The thinner, multicolored trajectory in each panel shows corresponding motion in the African plate frame of reference. Coastlines in each panel are as in (a), but for labelled ages.

upwind migration of plume material, against mantle flow below the lithosphere generated by the northeastward migrating African plate.

Lin et al. (2005) devised Cartesian models of mantle convection with a moving African plate and two stationary plumes — one beneath Afar and the other beneath Kenya — to explain the space-time distribution of magmatism in east Africa. This model with two fixed plumes, proposed to reconcile geochemical variation along the track of volcanic age-progression, is also problematic because the present-day tomographic images of the mantle under east Africa show no evidence of multiple distinct plumes (Montelli et al., 2006; French and Romanowicz, 2015).

With temperature scaled from seismic tomography, Conrad and Gurnis (2003) integrated regional convection models (with depth- and temperature-dependent viscosity) backwards in time and showed that a thermally buoyant structure beneath southern Africa generated 500–700 m of dynamic topography over the Cenozoic and that the center of uplift moved from eastern Africa to southern Africa since 30 Ma. In a similar study, Moucha and Forte (2011) integrated global convection models backwards in time to reconstruct the evolution of dynamic topography over the last 30 Myr. They initiate their models with mantle density perturbations derived from a mantle tomography model and employ a depth-dependent viscosity. Backward advection models, however, have limitations that restrict the time interval over which they can faithfully reproduce past mantle structures (Ismail-Zadeh et al., 2009). Critically, this time interval is short for conduction-dominated heat transfer, such as during the conductive thickening of the thermal boundary layer above the core mantle boundary (CMB), associated with plume nucleation. In other words, the evolution of the Afar plume since its nucleation to present-day cannot be fully captured by simple backward advection models. Consequently, the models in Conrad and Gurnis (2003) do not feature a plume eruption between 45 Ma and 30 Ma, associated with the onset of volcanism in east Africa, and the models in Moucha and Forte (2011) only go back to 30 Ma.

A more recent study (Koptev et al., 2015) used higher resolution models with a more complex rheology to explain the observed evolution of the central EARS through flow resulting from a fixed upper-mantle plume, directly beneath a craton subjected to far-field tensional stress. While Koptev et al. (2015) sought to explain how magmatic and amagmatic rifts can develop in identical tectonic environments, their study necessarily focused on a small segment of the broader EARS, thus excluding the effects of plume motion resulting from deep mantle flow regionally.

In this study, for the first time to our knowledge, we track motion of the model Afar plume in paleogeographically constrained spherical models of mantle convection that are integrated forward in time. We compare model plume trajectories to the age-progressive magmatism along EARS and investigate whether a moving Afar plume can reconcile constraints on the age-progression of magmatism and associated geochemical trends.

2. Methods

2.1. Governing equations for mantle convection

We consider spherical models of convection within the mantle under the extended-Boussinesq approximation (Christensen and Yuen, 1985;

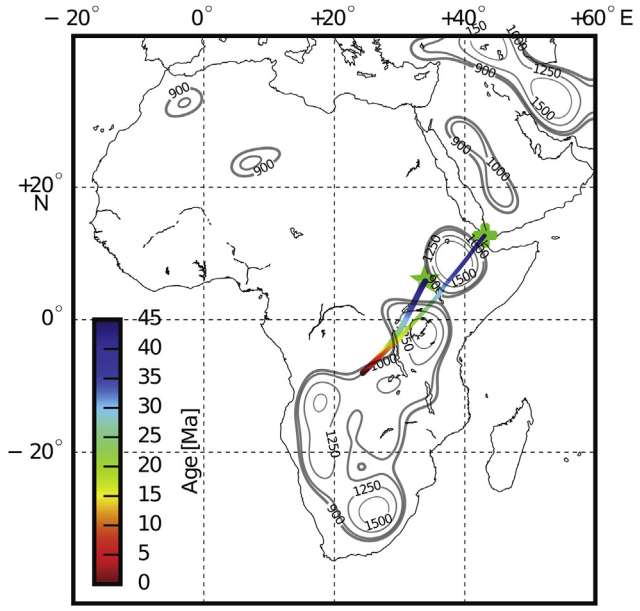

Fig. 5. Lateral motion of a synthetic Afar plume. The shorter, thicker trajectory, colored by age, shows the motion of a synthetic Afar plume (see section 2.6) — in mantle frame of reference — advected in the mean flow field of the deepest lower mantle in model M2. This trajectory starts from the eruption location of the Afar plume (see Fig. 1) and spans the last 45 Myr. The longer, thinner trajectory shows corresponding motion in the African plate frame of reference. Long-wavelength topographic contours are as those in Fig. 1a. The star and cross symbols in green are as described in Fig. 1b.

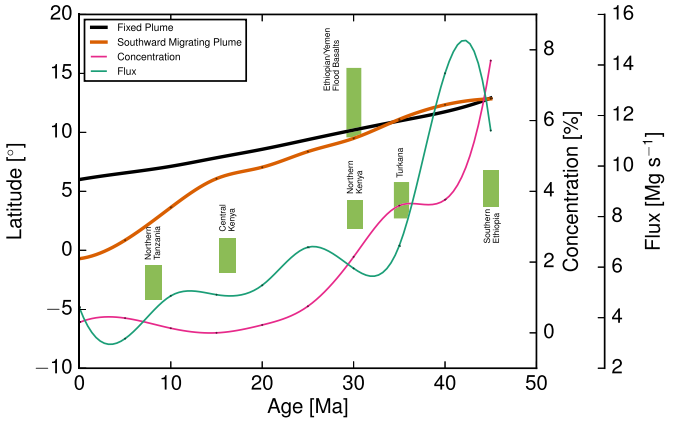

Fig. 6. A comparison of model plume location to observational constraints. The green rectangles mark the latitudinal extents of magmatism and the age progression since their onset from southern Ethiopia through Kenya into northern Tanzania (George et al., 1998). The black and orange curves show the latitudinal tracks created by a fixed Afar plume (Fig. 1) and the southward migrating Afar plume in model M2, respectively, beneath the northeastward migrating African plate. The magenta curve shows the evolution of the mean concentration of LLSVP material (as a percentage) within the plume conduit at a depth of 350 km. The cyan curve shows the evolution of plume flux at a depth of 350 km — see Hassan et al. (2015) for details on flux computation.

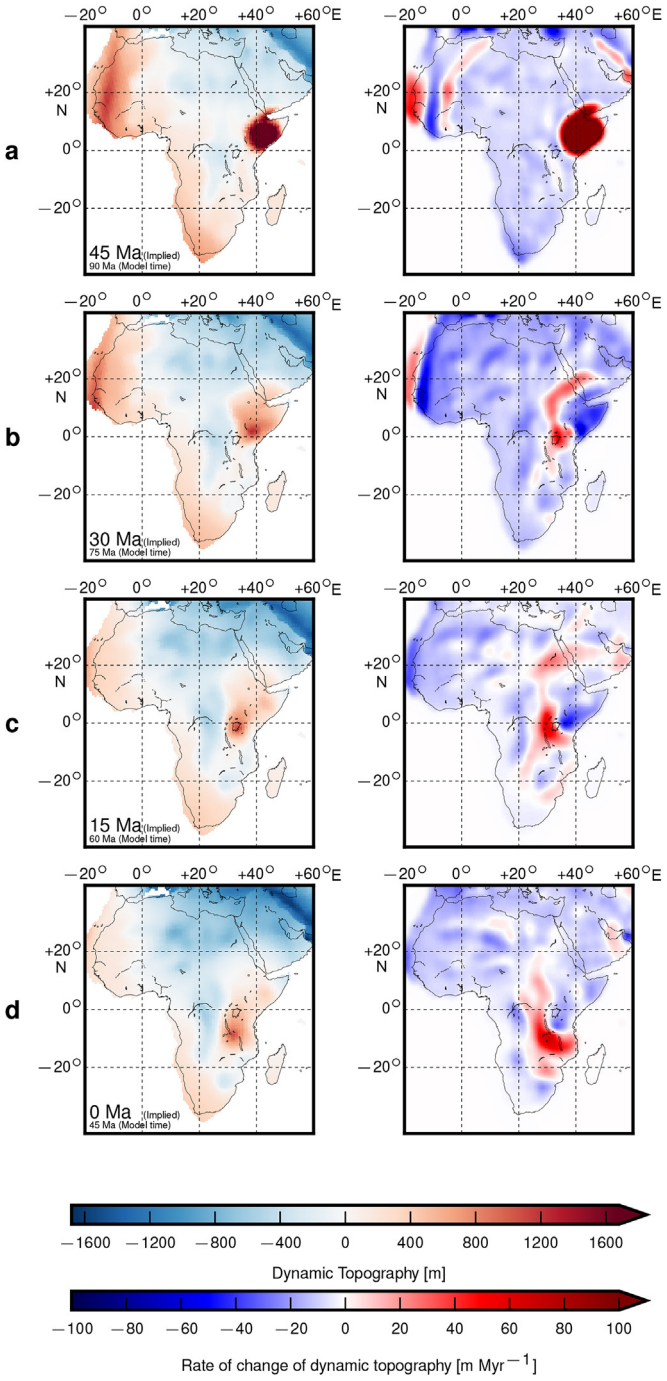

Fig. 7. Dynamic topography and its rate of change. Dynamic topography in model M2 in the African plate frame of reference at (a) 45 Ma, (b) 30 Ma, (c) 15 Ma and (d) 0 Ma are shown in the left panel and the rate of change are shown in the right panel.

Zhong, 2006). The nondimensional equations for the conservation of mass, momentum and energy are solved using the finite element method using CitcomS (Zhong et al., 2000, 2008; Bower et al., 2013).

Mass conservation in incompressible flow is given by:

$$\nabla \cdot u = 0 \tag{1}$$

where u is the velocity vector. Conservation of momentum is given by:

$$-\nabla P + \nabla \cdot \tau = (CB - \alpha T) g Ra e_r \tag{2}$$

where P, τ, C, B, α, T, Ra, g and e_r are the dynamic pressure, deviatoric stress tensor, compositional fraction, the ratio of chemical to thermal density anomaly, coefficient of thermal expansion, temperature, Rayleigh number, acceleration due to gravity and radial unit vector,

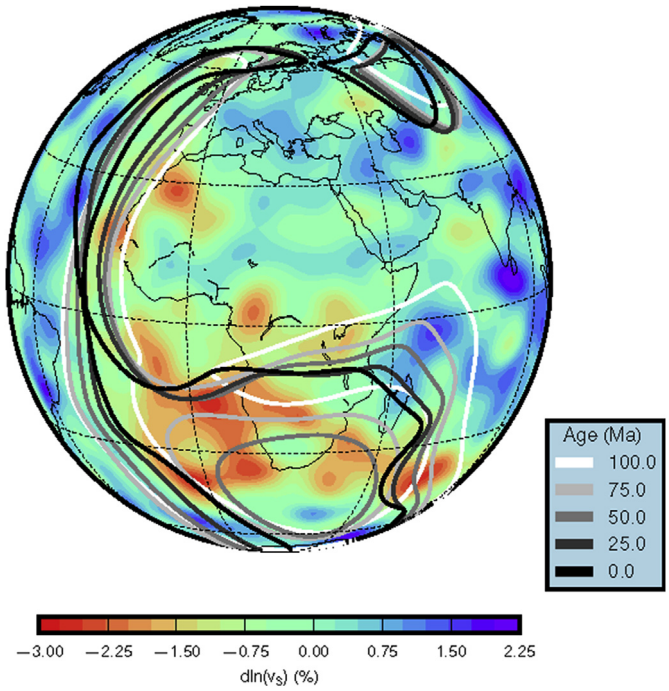

Fig. 8. Comparison of a tomography model to LLSVPs in model M2. SAVANI tomography model (Auer et al., 2014) at 2818 km depth is shown in the background. Contours of the 75% chemical concentration isosurface, 150 km above the CMB, show the evolution of the edges of the LLSVPs for model M2 (Table 2) over the last 100 Myr.

respectively. B is defined as:

$$B = \frac{\Delta\rho_{ch}}{\rho_0 \alpha_0 \Delta T} \tag{3}$$

where, $\Delta\rho_{ch}$, ρ_0 and ΔT are the chemical density anomaly, density, and the total temperature drop across the mantle, respectively. Quantities subscripted with '0' represent dimensional reference values. The Rayleigh number is defined as:

$$Ra = \frac{\rho_0 \alpha_0 \Delta T R_0^3 g_0}{\eta_0 \kappa_0} \tag{4}$$

where R_0, η_0, κ_0 are the radius of the Earth, viscosity and thermal diffusivity, respectively. Compared to the usual definition of *Ra*, here the radius of the Earth is used instead of the thickness of the mantle (this increases the normal *Ra* by nearly an order of magnitude).

The energy equation is given by:

$$c_p \frac{\partial T}{\partial t} = -c_p u \cdot \nabla T + \nabla \cdot \left(c_p \kappa \nabla T\right) - Di(T + T_s)\alpha g u_r + \frac{Di}{Ra}\tau : \dot{\varepsilon} + H \tag{5}$$

where c_p, Di, T_s, $\dot{\varepsilon}$ and H are the heat capacity at constant pressure, dissipation number, surface temperature, strain rate tensor and internal heating rate, respectively. The dissipation number, Di, is defined as:

$$Di = \frac{\alpha_0 g R_0}{c_p} \tag{6}$$

Chemical advection is governed by:

$$\frac{\partial C}{\partial t} + (u \cdot \nabla) C = 0 \tag{7}$$

Composition is advected using passive tracers (McNamara and Zhong, 2004). However, to limit the computational cost of advecting tracers, we restrict the number of tracers to 30 per element initially, guided by the recommendations based on resolution tests carried out in Van Keken et al. (1997) and Zhong et al. (2008). To further reduce computational cost, we remove ambient tracers between 410 km and 2600 km deep and impose $C = 0$ in elements with no tracers. Table 1 lists parameters kept fixed across all model cases.

We impose kinematic boundary conditions, derived from global plate tectonic reconstructions modified from Seton et al. (2012), in one million year intervals and linear interpolations in between. Plate velocities are extracted from these reconstructions with continuously closing plates (Gurnis et al., 2012) and exported using GPlates (Boyden et al., 2011). We also assimilate the thermal history of the lithosphere and shallow slabs. Following Flament et al. (2014), we use a half-space cooling model to derive a global temperature field of the lithosphere based on the global plate reconstruction in the oceans, and on tectonothermal ages (Artemieva, 2006) in the continents. A thermal model of slabs is constructed based on the reconstructed location and age of oceanic lithosphere at convergent plate margins. These slabs are initially inserted from the surface to a depth of 1200 km and slabs that appear during modelled geological time are progressively inserted into the upper mantle based on their age of appearance. This imposed thermal structure is blended with the dynamically evolving temperature field at each timestep — see Bower et al. (2013, 2015) for a more detailed description of the progressive data assimilation method. This approach captures the essential aspects of subduction through injecting slabs with realistic thickness and mass flux, without requiring complex rheological laws and computationally prohibitive finer model resolutions necessary to model the physics of plate boundaries.

2.2. Model setup

We build on earlier work (Hassan et al., 2015), where we systematically studied the influence of subduction-history and a chemically anomalous lower mantle on the nucleation of mantle plumes and their lateral motions, subsequent to eruption. Here, we adopt the same model setup and parameterizations for temperature-, composition- and depth-dependent viscosity law (leading to three orders of magnitude variations across the mantle), reference state, and internal heating as those in (Hassan et al., 2015). Similarly, composition-dependence of viscosity is restricted to the chemically distinct continents, whose thicknesses vary spatially depending on their tectonothermal age, as described in (Hassan et al., 2015) and references therein.

The initial condition at 230 Ma comprises a global temperature field that follows an *a priori* mantle adiabat, augmented by thermal boundary layers (TBLs) and cold slabs inserted to a given depth. The top and the bottom TBLs each encompass a temperature drop of 1225 K and the initial adiabatic temperature profile has a potential temperature of 1525 K. The initial condition also includes an anomalously dense layer that covers the CMB uniformly, in most model cases presented, except in model M6 (Table 2), in which the dense material is restricted to two antipodal and elongated domes, resembling present-day LLSVPs. We restrict the variation of the anomalous density across model cases to be within 2.5%–3.5%, guided by earlier studies that have shown that the long-term survival of the dense layer requires a positive density contrast in the range of 1%–6% compared to ambient mantle (Gurnis, 1986; Sleep, 1988; Tackley, 1998; Gonnermann et al., 2002; Samuel and Farnetani, 2003; Zhong and Hager, 2003; Tan and Gurnis, 2005). Across model cases, we also vary the initial thickness of the dense layer between 100 km and 150 km, to restrict the volume of the dense material to be comparable to estimates of the volume of LLSVPs (Burke et al., 2008; Hernlund and Houser, 2008).

At the CMB, we apply isothermal (nondimensional $T = 1$) and free-slip boundary conditions, while at the surface we impose isothermal (nondimensional $T = 0$) and kinematic boundary conditions. The kinematic boundary conditions are time-dependent and are derived from global plate tectonic reconstructions in 1 million year intervals and a linear interpolation in between. Because surface plate motions are a

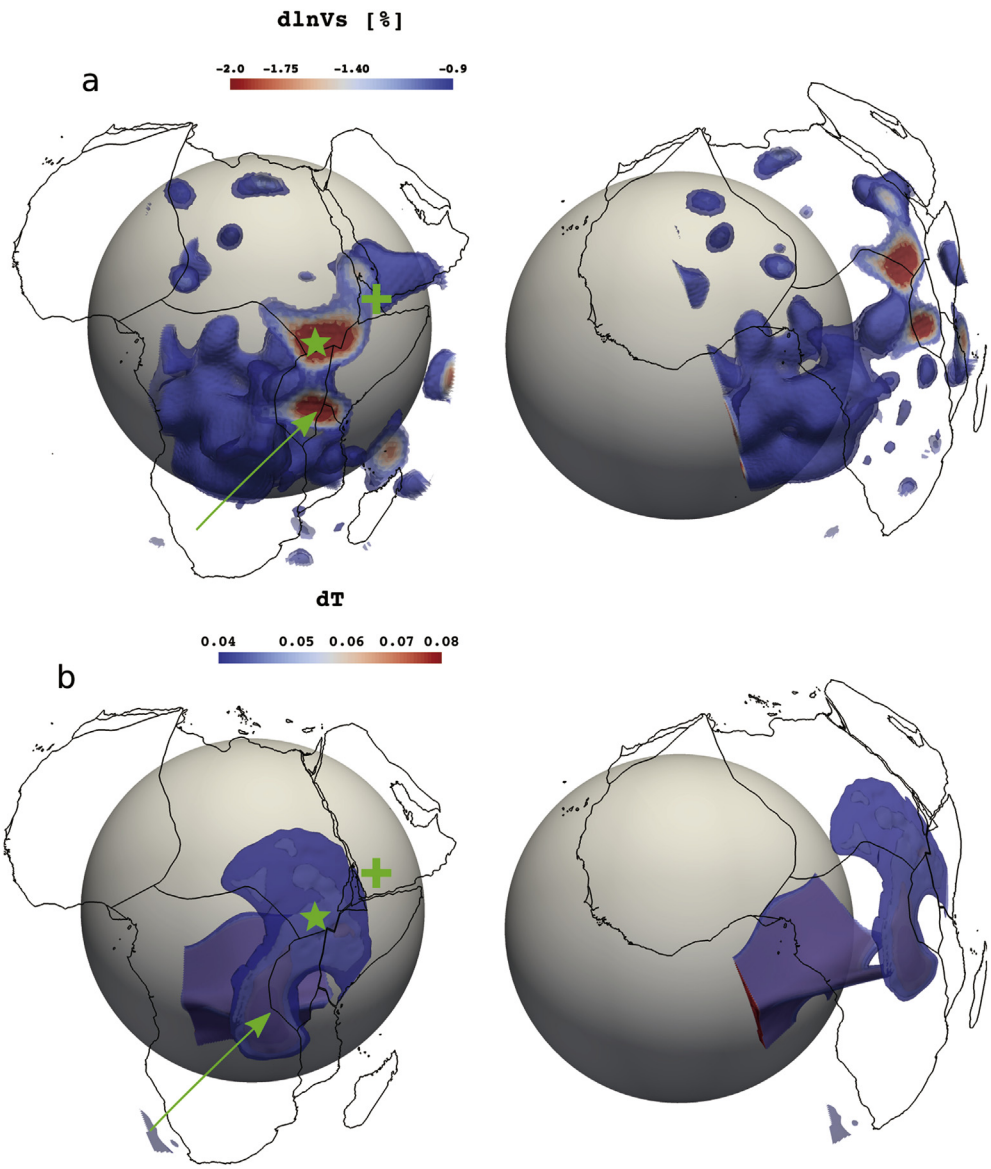

Fig. 9. Comparison of seismic tomography and model Afar plume. (a) Shear velocity (V_s) variations in model SEMUCB-WM1 (French and Romanowicz, 2015) are iso-surfaced at intervals of 0.25 within the range shown, for regions under present-day Africa, extending from 200 km below the surface to the CMB. The left and right panels show different perspectives in 3-dimensions. The Afar plume emerges from the deep lower mantle above the CMB (grey shell) and reaches the surface around the location marked by the green arrow. The star and cross symbols in green are as described in Fig. 1b. (b) The Afar plume in model M2 and its trail that formed between 90 Ma and 45 Ma is shown relative to the African plate reconstructed to 45 Ma based on APM1 — see section 4 for more details. The star and cross symbols in green are as described in Fig. 1b, but reconstructed similarly to 45 Ma. The non-dimensional temperature field, T, above layer averages is iso-surfaced at intervals of 0.04 within the range shown, delineating the model Afar plume and a trail of hot material left in its wake (see in text for more details). The left and right panels show different perspectives in 3-dimensions and the top 200 km is excluded from the rendering to avoid visual clutter.

function of both the absolute plate motion (APM) and relative plate motion (RPM) models, we use two alternative combinations of APM and RPM to assess their influences on mantle flow evolution. In both cases, we use the same RPM model from Seton et al. (2012), updated for circum-Arctic regions as described in Shephard et al. (2013). In the first instance, this RPM model is combined with an APM model constrained by lower mantle slab remnants (van der Meer et al., 2010), which we refer to as APM1. In the second instance, it is combined with an APM model described by Müller et al. (2016), which we refer to as APM2.

2.3. Dynamic topography

We compute time-dependent dynamic topography, h, at the surface at 5 Myr intervals as:

$$h = \frac{\sigma_{rr}}{\Delta\rho g} \tag{8}$$

where σ_{rr} and $\Delta\rho$ are the radial component of stress and the density difference between mantle and overlying material, respectively. The radial stresses, σ_{rr}, are recomputed, at each given time, using Stokes flow and the temperature field at that time. We exclude buoyancy in the top 250 km of the mantle in the Stokes solutions as we are focusing on the influence that deep plumes have on surface evolution. Additionally, the influences of traction induced by kinematic plate velocities are eliminated by imposing free-slip boundary conditions at the surface in these Stokes flow computations.

2.4. Poloidal flow in the deep lower mantle

Since the velocity field, u, in our convection models is incompressible (Eq.1), the tangential velocity field on each radial shell of the spherical mesh can be decomposed into poloidal and toroidal components. The poloidal component is related to buoyancy driven convergent or divergent flows, whereas the toroidal component is related to shearing and spinning motion, which originates from the combination of the buoyancy driven flow acting on lateral variations in viscosity and the kinematic boundary conditions at the surface. Following from Helmholtz's theorem on spheres (Backus, 1986),

$$\vec{V_s} = \nabla_s \Phi + \nabla_s \times (\Psi \vec{r}) \tag{9}$$

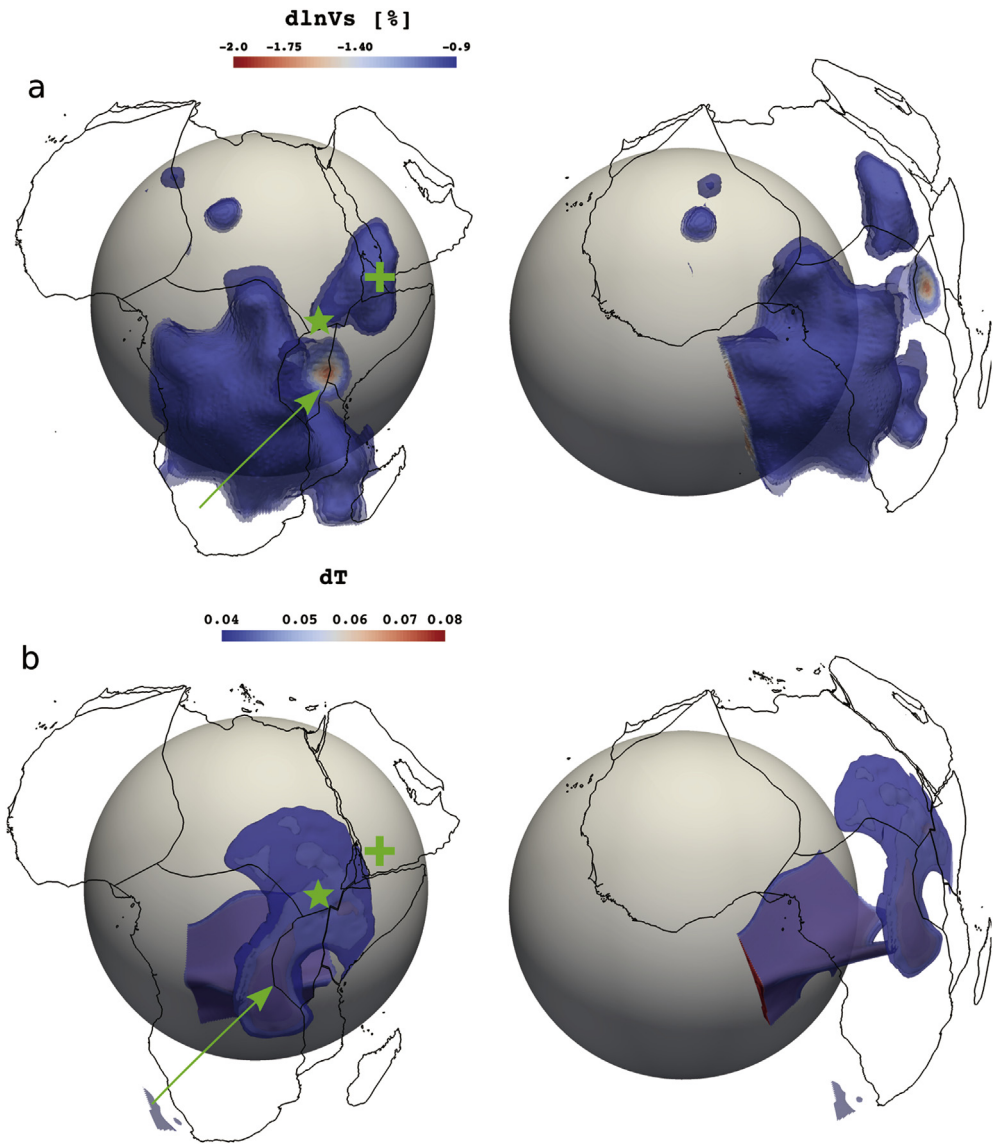

Fig. 10. Comparison of seismic tomography to model Afar plume. (a) Same as in Fig. 9a, but for SAVANI tomography model (Auer et al., 2014). (b) Same as in Fig. 9b.

where $\vec{V_s}$, ∇_s, Φ, Ψ and $\vec{r}$ are the tangential velocity on a radial shell of the computational domain, gradient operator on a spherical shell, poloidal potential, toroidal potential and radial unit vector. See Backus (1986) for more details.

The poloidal potential, Φ, is obtained as

$$\Phi = \nabla_s^{-2}(\nabla_s \cdot \vec{V_s}) \tag{10}$$

The poloidal flow field, V_p, on a radial shell is then obtained as

$$\vec{V_p} = \nabla_s \Phi \tag{11}$$

Time-averaged poloidal flow in the deepest lower mantle delineates regions of coherent flow relative to regions where flow is diffuse and is therefore an important indicator of past motions and differential deformations of LLSVPs.

2.5. Model hotspot tracks

Earlier Hassan et al. (2015), we developed a scheme for detecting plumes in global mantle convection models, based on cluster analysis of radial velocity fields. In order to identify model hotspot tracks, we post-process model outputs at 5 Myr intervals and compute a set of extant plume conduit locations, $S_t = \{P_i,\ldots,P_n\}$, at a depth of 350 km based on the plume detection scheme. Subscript n denotes the total number of plumes detected at model time t. A collection of age-progressive model hotspot tracks are then identified by binning conduit locations from the ensemble set $S = \{S_{t_0},\ldots,S_{t_m}\}$ based on spatiotemporal proximity, where t_0 is the model time when the first model plumes appear and t_m is the model time corresponding to the present-day. These age-progressive hotspot tracks in the mantle frame of reference are then 'reverse-reconstructed' to the plate frame of reference using GPlates (Boyden et al., 2011) to facilitate direct comparisons with observations.

2.6. Advection of synthetic plumes

The spatial distribution of model plume eruption locations — i.e. locations where model plumes impinge below the lithosphere — is correlated with reconstructed eruption locations of large igneous provinces (LIPs) at a statistically significant level (Hassan et al., 2015). A large selection of models formulated with reasonable parameters (Hassan et al., 2015, 2016) demonstrate that flow characteristics in the deepest lower mantle render certain regions more conducive to plume nucleation, which we refer to here as robust plume nucleation sites. Moreover,

there is a close correspondence of a number of model plumes, at present-day, to seismically observed plumes of deep origin (see Fig. 11a in Hassan et al. (2015)). Most model plumes erupt near the surface between 160 Ma and 60 Ma, depending on model parameters. Although the average transit time of an incipient plume from the CMB to the surface depends on model parameters, e.g. the viscosity, Rayleigh number, etc., the exact timing of a model plume nucleating near a robust plume nucleation site seems partially stochastic. This often complicates comparing model predictions to observations, even when general trends — e.g. rate of age progression in hotspot tracks and rate of change of plume-induced dynamic topography — in both are broadly in agreement.

This difficulty is partially overcome with a scheme that interrogates convection models and computes synthetic trajectories for seismically observed plumes that erupted at precise space-time locations, not found in the models. Analogous to Steinberger (2000), we advect roots of potential plumes in the evolving flow field of the deepest lower mantle in a given model, as a post-processing step. This allows assessment of potential trajectories of a seismically observed plume since its eruption, in order to establish whether a model plume separated from it by a small space-time offset can be adopted as its proxy. The advection is carried out in the mean flow field within a 300 km thick shell above the CMB using a fourth-order Runge-Kutta scheme. We refer to such plumes as synthetic plumes. In section 4 we elaborate further on the rationale behind how the thermochemical evolution and the space-time varying dynamic topography associated with a model plume can be related to the observed Afar plume despite there being a space-time offset between them.

3. Results

We present a total of six cases computed from 230 Ma to the present, where we varied the thickness and geometry of the initial dense layer above the CMB, its anomalous density ($\Delta\rho_{ch}$) and the absolute plate motion (APM) model used to derive kinematic boundary conditions (see section 2.2), keeping all other parameters constant. The parameters for each model case and the age of eruption of the model Afar plume are given in Table 2.

3.1. Southward migration of the Afar plume

Within ~50 Myr of the start of models M1–M5, the dense material above the CMB in these models forms two separate structures that evolve to resemble the shapes of present-day LLSVPs under Africa and the Pacific, implying that these structures could be relatively young geologically with location and geometry that is a product of subduction geometry during Pangea's assembly and subsequent breakup. However, as a pre-Mesozoic dense layer may have already been deformed and displaced by descending slabs, we initiate model M6 with two separate domes of dense material that are similar in shape and volume to present-day LLSVPs to explore this scenario. These domes are ~1000 °C higher in temperature than ambient mantle. Hereafter we refer to these thermochemical structures in the models as LLSVPs, interchangeably.

Mantle plumes emerge mostly from the edges of LLSVPs (Burke et al., 2008) — a phenomenon that has been reproduced in a number of modelling studies (Tan et al., 2011; Steinberger and Torsvik, 2012; Bower et al., 2013; Hassan et al., 2015), which also suggest that LLSVPs can migrate laterally due to subduction-induced flow in the deep lower mantle. Earlier Hassan et al. (2015) we have shown that as LLSVPs and their edges migrate, so do plumes anchored to them.

We compute the poloidal component of the mean flow field in a 300 km thick shell above the CMB in each model, at 5 Myr intervals. The viscosity within this layer is low due to elevated temperatures in the thermal boundary layer above the CMB (Olson et al., 1987), which facilitates motion of plume roots. The flow patterns affecting African LLSVP morphology are coherent over the last 100 Myr (well-illustrated by time-averaged poloidal flow, Fig. 2). All model cases show an equatorial band of strong southward flow in the deep lower mantle under present-day Africa, which results from the consistent pattern of subduction further north. This coherent flow pushed the African LLSVP southward, along with the Afar plume, which is anchored to the edge of the LLSVP (Fig. 3). This is consistent with earlier studies that showed that return flow in the deep lower mantle can cause plumes to migrate laterally in a direction opposite to associated plate motion (Olson, 1987; Steinberger and O'Connell, 1998).

In the mantle frame of reference, the model Afar plume moves southwestward in each model (Fig. 2). The southward component of the motion of the model Afar plume is more restricted in models M3 and M4 (Fig. 2c and d), likely due to the initially thicker chemical layer (Table 2). The coherent band of flow under Africa in model M6 is wider compared to other models and is likely because the dense chemical layer is dome-shaped in the initial condition, which could facilitate lateral motion of descending slabs. Nonetheless, the extent of southward motion of the Afar plume in model M6 is comparable to those in models where the dense chemical layer is initially 100 km thick (Table 2). The motion of the model Afar plume in models M3–M6 feature a more pronounced longitudinal component, compared to those in models M1 and M2 (Fig. 2) — a consequence of the APM models used in the corresponding models, since the APM models used have a first order control over the location of subduction zones through time. Since LLSVPs in models that incorporate APM1 provide a better match to seismically observed LLSVPs (Steinberger and Torsvik, 2012), and because the Afar plume erupts closer to 45 Ma in model M2 (compared to that in model M1), we chose M2 as the preferred model.

4. Discussion

The earliest volcanism associated with the Afar plume occurred ~45 Ma, however, the Afar plume in the models erupts much earlier (~75–115 Ma; Table 2). While the exact timing of model plume eruptions is partly the outcome of a stochastic process (see section 2.6), the temporal offset between the eruption of the model Afar plume in all model cases and the onset of earliest volcanism in east Africa at ~45 Ma could also partly be a consequence of the simplified bottom thermal boundary layer and the uniform depth to which preexisting slab material are incorporated in the initial conditions (see sections 2.1 and 2.2). The model Afar plume in the preferred model (M2) erupts under east Africa at 90 Ma when Africa was further south compared to that at 45 Ma. The eruption location of the model plume and its subsequent southwestward migration is shown in Fig. 4, both in mantle and African plate frames of references.

The general flow patterns in the deep lower mantle under Africa have remained coherent over the last 100 Myr, as shown by the equatorial band of strong southward flow under Africa (Fig. 2). We conclude that if the general flow patterns in the deep lower mantle remain coherent over long periods regionally, motion of plume-roots within such space-time windows are expected to follow a similar trajectory. Thus, the root of the observed Afar plume that erupted at ~45 Ma should follow a similar southwestward trajectory as those in Fig. 4d.

We consider the motion of a synthetic plume between 45 Ma and present-day, to access whether the evolution and motion of the model Afar plume between 90 Ma and 45 Ma can be adopted as a proxy for that of the observed Afar plume between 45 Ma and present-day. We advect a synthetic plume root (see section 2.6), starting from the eruption location of the Afar plume (see Fig. 1b) at 45 Ma, towards present day based on the flow field of the lowermost mantle in model M2 (Fig. 5 shows the motion of the synthetic Afar plume in both mantle and African plate frames of references). We observe a broad agreement between the motion paths of the model plume (Fig. 4d) and those of the synthetic plume (Fig. 5). However, the extent of motion of the model plume, both in the mantle and African plate frames of references, is more subdued compared to that of the synthetic plume. Such differences are not unexpected as the synthetic plumes are advected through the mean flow field of the lowermost mantle and thus produce smoother trajectories, while actual

model plume motion can be more intricate, but still conforming to general trends observed for a corresponding synthetic plume. Based on this consistency of motion trajectories of the synthetic and model Afar plumes, we adopt the evolution and motion of the model Afar plume between 90 Ma and 45 Ma as a proxy for those of the observed Afar plume between 45 Ma and present-day.

However, we stress that because the model plume eruption location does not coincide with the observed eruption location of the Afar plume and partly because the relative position of Africa above the African LLSVP between 90 Ma and 45 Ma is different to that between 45 Ma and present-day, a detailed comparison of geochemical trends and dynamic topography to established observational constraints is precluded in the analysis. The comparisons presented in the following sections should instead serve as clues towards piecing together a consistent geodynamic framework for the evolution of East Africa.

4.1. Comparison to geochemical and magmatic history

The clear contrast between the hotspot track in Fig. 4d and the hotspot track created by a fixed Afar plume on the African plate (Fig. 1a and b) suggests that a moving Afar plume may explain the space-time distribution of magmatism better than a model with one fixed plume (Ebinger and Sleep, 1998), or that with two fixed plumes (George et al., 1998; Lin et al., 2005; Rogers, 2006). We observe a clear latitudinal trend between the observed age-progressive volcanism and the location of the model Afar plume (orange curve in Fig. 6) in an African plate frame of reference. This demonstrates that the apparent motion of the surface expression of the model plume — resulting from the effects of both plume and plate motion — is more consistent with the paleomagnetic record of the observed volcanism, compared to that predicted by a stationary plume (black curve in Fig. 6).

The volcanism along the entire EARS, including the formation of its eastern and western branches could be potentially explained by a single southward migrating Afar plume (Fig. 6); however, the onset of magmatism associated with the Ethiopian and Yemen flood basalts appears as an exception to the latitudinal trend. Continental flood basalts can erupt away from the plume axis depending on local factors such as lithospheric thickness and preexisting weaknesses (Ebinger and Sleep, 1998) and we suggest that the Ethiopian and Yemen flood basalts resulted from peak magmatism associated with a burst in lateral flow of plume material that occurred subsequent to plume eruption. This is demonstrated by the model Afar plume reaching peak plume flux subsequent to eruption (cyan curve in Fig. 6) — however, this delay is smaller compared to our interpretation of the observed magmatic events regionally. We also note that the present-day model plume flux (Fig. 6) is comparable to the constant flux value used for the Afar plume in Ebinger and Sleep (1998).

Northern Ethiopian flood basalts constitute the most voluminous magmas that were generated at greater depths and higher temperatures, compared to the Eocene Amaro basalts of southern Ethiopia (Rogers, 2006). Furthermore, the Ethiopian and Kenyan portions of EARS have chemically distinct source regions, as inferred from regional patterns of Pb and He isotopic composition (Furman, 2007). Earlier numerical studies have shown that large contrasts in helium isotopic signatures can result from mantle plumes sampling the denser, relatively undegassed basal layer and the overlying degassed mantle (Samuel and Farnetani, 2003). Distinct lower mantle components can ascend through a plume conduit and preserve their isotopic signature in erupted basalts. A salient feature of the model plume evolution is the sharp decrease in the concentration of denser LLSVP material within the conduit since eruption, which suggests that as the plume flux diminishes, the plume samples progressively shallower parts of the deep mantle (Fig. 6). This may explain the systematic geochemical variation between the northern Ethiopian basalts and the more recent basalts that erupted in the Kenya rift (Rogers, 2006; Furman, 2007).

4.2. Comparison to uplift history

The dynamic topography in our preferred model M2 and its rate of change, $\dot{h}$, with the temporal shift applied, both evolve over Africa as described earlier (Fig. 7). The domal uplift generated at the time of eruption (Fig. 7a) has a radius of ~700 km and an amplitude in excess of 1200 m, comparable to inferred uplift (He et al., 2003; Pik et al., 2003, 2008; Burke and Gunnell, 2008). The surface expression of the model Afar plume then migrates southward by ~15°, with the fastest motion occurring since 15 Ma (Fig. 7). The topographic swell associated with the plume, subsequent to eruption, has an amplitude that ranges of ~800–1000 m and the plume gradually weakens as it arrives beneath southern Tanzania at present-day (see plume flux in Fig. 6), leaving a trail of subsiding regions in its wake (Fig. 7). The space-time varying uplift and its rate of change (Fig. 7) are comparable to those presented in Moucha and Forte (2011) and Conrad and Gurnis (2003). We note that the time-varying spatial extent and amplitude of uplift associated with the surface expression of the plume is likely to have caused major drainage reorganizations, as suggested for the region (Pik et al., 2003; Goudie, 2005; Stankiewicz and de Wit, 2005; Roberts et al., 2012; Underwood et al., 2013).

At present-day, the most prominent broad peak in surface dynamic topography in our preferred model M2 is centered on the Tanzania Craton (Fig. 7). This agrees well with the residual topography of eastern Africa, which is also dominated by a peak in the same region (Nyblade and Robinson, 1994). In contrast, the present-day dynamic topography model by Moucha and Forte (2011) produces a broad NNE–SSW-oriented positive dynamic topography feature centered on the Afar triangle, in disagreement with residual topography.

Adopting the evolution of the model Afar plume between 90 Ma and 45 Ma as a proxy for the evolution of the observed Afar plume since 45 Ma is not ideal, because although this approach allows for broad comparisons with geological observations, the long-wavelength dynamic topography of the African continent between 90 Ma and 45 Ma is different from that between 45 Ma and present-day. This is partly due to the location of the African plate relative to the underlying LLSVP over these two different time windows. We also note that plume-related uplift obtained in numerical studies of plume-lithosphere interactions vary widely; models with simple rheological setups (e.g. Ribe and Christensen (1994)), as adopted in this study, reproduce long-wavelength topographic swells better, whereas more recent studies argue that with complex rheologies, both the wavelength and amplitude of uplift can be strongly modulated (Burov and Guillou-Frottier, 2005; Burov and Gerya, 2014). Furthermore, shallow mantle processes such as plume-triggered delamination of deep lithospheric roots that have been shown to explain a fraction of the high topography in the region (Hu et al., 2018) are not included in our models. We therefore suggest that dynamic topography and its rate of change in Fig. 7 should be interpreted with caution.

4.3. Comparison to seismic tomography

The steady pattern of subduction associated with the closure of the Tethys produces coherent lower mantle flow (Fig. 2) and it has a first order control on the morphology of the African LLSVP. The eastern edges of the African LLSVP migrated southwestward as a consequence (Fig. 8). This is consistent with inferences from studies that suggest that the deformation of edges of the African LLSVP is concentrated under present-day east Africa (Lynner and Long, 2014) — furthermore, shear wave splitting measurements that sample the eastern edge of the African LLSVP are consistent with mantle flow models that predict a southwesterly flow under east Africa (Ford and Long, 2015; Reiss et al., 2019). The present-day model African LLSVP compares reasonably well with the low shear velocity regions in a tomography model (Fig. 8). In particular, the

strongest shear velocity perturbations beneath southern Africa agree well with the edges of the model African LLSVP there at present-day.

Global tomographic studies (Montelli et al., 2004, 2006; French and Romanowicz, 2015) show that the putative present-day location of the Afar plume does not feature a contiguous plume conduit, extending to the lower mantle vertically below (Figs. 9a and 10a), unlike other robust plumes, and instead, the Afar plume has been suggested to be an extension of the African LLSVP (Montelli et al., 2006), corroborated by cross-sections through a number of tomography models (French and Romanowicz (2015) Extended Data Fig. 3). Although a plume may have once been active under the Afar rift system, thermal influence of a plume directly beneath Afar at present-day is minimal (Rychert et al., 2012) and regional tomographic studies also suggest a deep mantle source of magmatism (Chang and Ven der Lee, 2011; Civiero et al., 2015, 2016), without a contiguous connection to the deep lower mantle vertically below.

A comparison of two recent tomography models (Figs. 9a and 10a) to the model Afar plume in our preferred model M2 (Fig. 9b) suggests a close correspondence not only between the extent of trailing plume material, but also its general trajectory. This suggests that the trail of hot material underlying EARS, as imaged in seismic tomography, are relics of the Afar plume that migrated southward since eruption.

5. Conclusion

We have presented a detailed analysis of a model Afar-like plume that migrates southwards, guided by deep lower mantle flow regimes that have persisted over the last 100 Myr near the eastern edges of the African LLSVP. We surmise that the evolution of the thermochemical signature of the model plume and its associated uplift history is broadly representative of the observed Afar plume. The method presented here is a necessary compromise that allows us to interrogate fully dynamic model plumes that evolve in a global flow field, to glean insights into the evolution of observed plumes. While our approach mitigates the limitations inherent in backward advection models (Conrad and Gurnis, 2003; Moucha and Forte, 2011), moderate to large space-time offsets between the eruption of model plumes near robust plume nucleation sites and corresponding observed plumes could potentially limit its applicability. Further work is required in developing a robust mechanism for optimizing model parameters along with initial conditions to systematically reduce space-time offsets between the eruption of model and observed plumes.

Although the double-plume model (George et al., 1998; Rogers, 2006) was proposed to reconcile geochemical data, it has not proven consistent with all observational constraints, particularly the propagation of plume material from southern Ethiopia towards Afar, in a direction opposite to that predicted by plate motion over a fixed plume (Rogers, 2006). On the other hand, our analysis suggests that a southward moving Afar plume, consistent with lower mantle flow regimes under Africa since 45 Ma, better explains age-progressive volcanism over the same period in EARS. A fully dynamic model Afar plume, presented in this study, shows that plume flux can reach its peak subsequent to eruption, which may explain the onset of magmatism associated with the Ethiopian and Yemen flood basalts at 30 Ma. We suggest that as the model plume weakens over its lifetime, it samples progressively shallower parts of the deep mantle, which could explain the systematic geochemical variation observed in the age-progressive magmatism. Our results have implications for better understanding the link between the history of subduction, deep mantle dynamics, plume seeding and advection and plume-lithosphere interaction. Better understanding these links will lead to improved interpretations of the geodynamic evolution of EARS and consequently, the geomorphological evolution of paleo-drainage systems in east Africa.

Declaration of competing interest

The authors declare that they have no known competing financial interests or personal relationships that could have appeared to influence the work reported in this paper.

Acknowledgments

We obtained CitcomS (version 3.2) from the Computational Infrastructure for Geodynamics (http://geodynamics.org/). GPlates (http://www.gplates.org/) is developed at the University of Sydney, the California Institute of Technology and the Geological Survey of Norway. This research was supported by ARC grants IH130200012 and DP130101946 and MG was supported by the National Science Foundation under award EAR-1645775. This research was undertaken with the assistance of resources from the National Computational Infrastructure (NCI), which is supported by the Australian Government. An earlier draft of the manuscript benefited from reviews by Clinton Conrad and two anonymous reviewers.

References

Amante, C., Eakins, B.W., 2009. ETOPO1 1 Arc-Minute Global Relief Model: Procedures, Data Sources and Analysis. US Department of Commerce, National Oceanic and Atmospheric Administration, National Environmental Satellite, Data, and Information Service, National Geophysical Data Center, Marine Geology and Geophysics Division Colorado.

Artemieva, I.M., 2006. Global 1× 1 thermal model tc1 for the continental lithosphere: implications for lithosphere secular evolution. Tectonophysics 416 (1), 245–277.

Auer, L., Boschi, L., Becker, T., Nissen-Meyer, T., Giardini, D., 2014. Savani: a variable resolution whole-mantle model of anisotropic shear velocity variations based on multiple data sets. J. Geophys. Res.: Solid Earth 119 (4), 3006–3034.

Backus, G., 1986. Poloidal and toroidal fields in geomagnetic field modeling. Rev. Geophys. 24 (1), 75–109.

Bower, D.J., Gurnis, M., Flament, N., 2015. Assimilating lithosphere and slab history in 4-D Earth models. Phys. Earth Planet. Inter. 238, 8–22.

Bower, D.J., Gurnis, M., Seton, M., Jan. 2013. Lower mantle structure from paleogeographically constrained dynamic Earth models. Geochem. Geophys. Geosyst. 14 (1), 44–63. https://doi.org/10.1029/2012GC004267.

Boyden, J.A., Müller, R.D., Gurnis, M., Torsvik, T.H., Clark, J.A., Turner, M., Ivey-Law, H., Watson, R.J., Cannon, J.S., 2011. Next-generation plate-tectonic reconstructions using GPlates. Geoinformatics: cyberinfrastructure for the solid earth sciences 95–114.

Burke, K., 1996. The African plate. S. Afr. J. Geol. 99 (4), 341–409.

Burke, K., Gunnell, Y., 2008. The African erosion surface: a continental-scale synthesis of geomorphology, tectonics, and environmental change over the past 180 million years. Geol. Soc. Am. Mem. 201, 1–66.

Burke, K., Steinberger, B., Torsvik, T.H., Smethurst, M.A., 2008. Plume generation zones at the margins of large low shear velocity provinces on the core–mantle boundary. Earth Planet. Sci. Lett. 265 (1), 49–60.

Burov, E., Gerya, T., 2014. Asymmetric three-dimensional topography over mantle plumes. Nature 513 (7516), 85–89.

Burov, E., Guillou-Frottier, L., 2005. The plume head–continental lithosphere interaction using a tectonically realistic formulation for the lithosphere. Geophys. J. Int. 161 (2), 469–490.

Chang, S.-J., Van der Lee, S., 2011. Mantle plumes and associated flow beneath Arabia and east Africa. Earth Planet. Sci. Lett. 302 (3), 448–454.

Christensen, U.R., Yuen, D.A., 1985. Layered convection induced by phase transitions. J. Geophys. Res.: Solid Earth 90 (B12), 10291–10300, 1978–2012.

Civiero, C., Goes, S., Hammond, J.O., Fishwick, S., Ahmed, A., Ayele, A., Doubre, C., Goitom, B., Keir, D., Kendall, J.M., Leory, S., Ogubazghi, G., Rumpker, G., Stuart, G.W., 2016. Small-scale thermal upwellings under the northern east African rift from s travel time tomography. J. Geophys. Res.: Solid Earth 121 (10), 7395–7408.

Civiero, C., Hammond, J.O., Goes, S., Fishwick, S., Ahmed, A., Ayele, A., Doubre, C., Goitom, B., Keir, D., Kendall, J., Leory, S., Ogubazghi, G., Rumpker, G., Stuart, G.W., 2015. Multiple mantle upwellings in the transition zone beneath the northern east-African rift system from relative p-wave travel-time tomography. Geochem. Geophys. Geosyst. 16 (9), 2949–2968.

Conrad, C.P., Gurnis, M., 2003. Seismic tomography, surface uplift, and the breakup of gondwanaland: integrating mantle convection backwards in time. Geochem. Geophys. Geosyst. 4 (3). https://doi.org/10.1029/2001GC000299.

Ebinger, C., Bechtel, T., Forsyth, D., Bowin, C., 1989. Effective elastic plate thickness beneath the east African and Afar plateaus and dynamic compensation of the uplifts. J. Geophys. Res.: Solid Earth 94 (B3), 2883–2901.

Ebinger, C.J., Sleep, N., 1998. Cenozoic magmatism throughout east Africa resulting from impact of a single plume. Nature 395 (6704), 788–791.

Flament, N., Gurnis, M., Williams, S., Seton, M., Skogseid, J., Heine, C., Dietmar Müller, R., 2014. Topographic asymmetry of the south Atlantic from global models of mantle flow and lithospheric stretching. Earth Planet. Sci. Lett. 387, 107–119.
Ford, H.A., Long, M.D., 2015. A regional test of global models for flow, rheology, and seismic anisotropy at the base of the mantle. Phys. Earth Planet. Inter. 245, 71–75.
French, S.W., Romanowicz, B., 2015. Broad plumes rooted at the base of the earth's mantle beneath major hotspots. Nature 525 (7567), 95–99.
Furman, T., 2007. Geochemistry of east African rift basalts: an overview. J. Afr. Earth Sci. 48 (2–3), 147–160.
George, R., Rogers, N., Kelley, S., 1998. Earliest magmatism in Ethiopia: evidence for two mantle plumes in one flood basalt province. Geology 26 (10), 923–926.
Gonnermann, H.M., Manga, M., Mark Jellinek, A., 2002. Dynamics and longevity of an initially stratified mantle. Geophys. Res. Lett. 29 (10), 33–1.
Goudie, A.S., 2005. The drainage of Africa since the Cretaceous. Geomorphology 67 (3), 437–456.
Gurnis, M., 1986. The effects of chemical density differences on convective mixing in the Earth's mantle. J. Geophys. Res. 91, 11407–11419.
Gurnis, M., Mitrovica, J.X., Ritsema, J., van Heijst, H.-J., 2000. Constraining mantle density structure using geological evidence of surface uplift rates: the case of the African superplume. Geochem. Geophys. Geosyst. 1 (7). https://doi.org/10.1029/2005gc000928.
Gurnis, M., Turner, M., Zahirovic, S., DiCaprio, L., Spasojevic, S., Müller, R.D., Boyden, J., Seton, M., Manea, V.C., Bower, D.J., 2012. Plate tectonic reconstructions with continuously closing plates. Comput. Geosci. 38 (1), 35–42.
Hassan, R., Flament, N., Gurnis, M., Bower, D.J., Müller, D., 2015. Provenance of plumes in global convection models. Geochem. Geophys. Geosyst. 16 (5), 1465–1489.
Hassan, R., Müller, R.D., Gurnis, M., Williams, S.E., Flament, N., 2016. A rapid burst in hotspot motion through the interaction of tectonics and deep mantle flow. Nature 533 (7602), 239–242.
He, B., Xu, Y.-G., Chung, S.-L., Xiao, L., Wang, Y., 2003. Sedimentary evidence for a rapid, kilometer-scale crustal doming prior to the eruption of the Emeishan flood basalts. Earth Planet. Sci. Lett. 213 (3), 391–405.
Hernlund, J.W., Houser, C., 2008. On the statistical distribution of seismic velocities in Earth's deep mantle. Earth Planet. Sci. Lett. 265 (3), 423–437.
Hu, J., Liu, L., Faccenda, M., Zhou, Q., Fischer, K.M., Marshak, S., Lundstrom, C., 2018. Modification of the western Gondwana craton by plume–lithosphere interaction. Nat. Geosci. 11 (3), 203.
Ismail-Zadeh, A., Korotkii, A., Schubert, G., Tsepelev, I., 2009. Numerical techniques for solving the inverse retrospective problem of thermal evolution of the Earth interior. Comput. Struct. 87 (11), 802–811.
Koptev, A., Calais, E., Burov, E., Leroy, S., Gerya, T., 2015. Dual continental rift systems generated by plume-lithosphere interaction. Nat. Geosci. 8 (5), 388.
Lin, S.-C., Kuo, B.-Y., Chiao, L.-Y., Van Keken, P.E., 2005. Thermal plume models and melt generation in east Africa: a dynamic modeling approach. Earth Planet. Sci. Lett. 237 (1), 175–192.
Lithgow-Bertelloni, C., Silver, P.G., 1998. Dynamic topography, plate driving forces and the African superswell. Nature 395 (6699), 269–272.
Lynner, C., Long, M.D., 2014. Lowermost mantle anisotropy and deformation along the boundary of the African LLSVP. Geophys. Res. Lett. 41 (10), 3447–3454.
McNamara, A.K., Zhong, S., 2004. Thermochemical structures within a spherical mantle: Superplumes or piles? J. Geophys. Res.: Solid Earth 109 (B7). https://doi.org/10.1029/2003JB002847 n/a–n/a.
Montelli, R., Nolet, G., Dahlen, F., Masters, G., 2006. A catalogue of deep mantle plumes: new results from finite-frequency tomography. Geochem. Geophys. Geosyst. 7 (11) https://doi.org/10.1029/2006GC001248.
Montelli, R., Nolet, G., Dahlen, F., Masters, G., Engdahl, E.R., Hung, S.-H., 2004. Finite-frequency tomography reveals a variety of plumes in the mantle. Science 303 (5656), 338–343.
Moucha, R., Forte, A.M., 2011. Changes in African topography driven by mantle convection. Nat. Geosci. 4 (10), 707–712.
Müller, R.D., Seton, M., Zahirovic, S., Williams, S.E., Matthews, K.J., Wright, N.M., Shephard, G.E., Maloney, K.T., Barnett-Moore, N., Hosseinpour, M., Bower, D.J., Cannon, J., 2016. Ocean basin evolution and global-scale plate reorganization events since Pangea breakup. Annu. Rev. Earth Planet Sci. 44, 107–138.
Nelson, W., Furman, T., Hanan, B., 2008. Sr, Nd, Pb and Hf evidence for two-plume mixing beneath the east African rift system. Geochem. Cosmochim. Acta 72, A676.
Nyblade, A.A., Robinson, S.W., 1994. The African superswell. Geophys. Res. Lett. 21 (9), 765–768.
Olson, P., 1987. Drifting mantle hotspots. Nature 327 (6123), 559–560.
Olson, P., Schubert, G., Anderson, C., 1987. Plume formation in the d"-layer and the roughness of the core–mantle boundary. Nature 327 (6121), 409–413.
Pik, R., Marty, B., Carignan, J., Lavé, J., 2003. Stability of the upper nile drainage network (Ethiopia) deduced from (U–Th)/He thermochronometry: implications for uplift and erosion of the Afar plume dome. Earth Planet. Sci. Lett. 215 (1), 73–88.
Pik, R., Marty, B., Carignan, J., Yirgu, G., Ayalew, T., 2008. Timing of east African rift development in southern Ethiopia: implication for mantle plume activity and evolution of topography. Geology 36 (2), 167–170.
Reiss, M., Long, M., Creasy, N., 2019. Lowermost mantle anisotropy beneath Africa from differential SKS-SKKS shear-wave splitting. J. Geophys. Res.: Solid Earth 124 (8), 8540–8564.
Ribe, N., Christensen, U., 1994. Three-dimensional modeling of plume-lithosphere interaction. J. Geophys. Res.: Solid Earth 99 (B1), 669–682.
Roberts, E.M., Stevens, N., O'connor, P., Dirks, P., Gottfried, M.D., Clyde, W., Armstrong, R., Kemp, A., Hemming, S., 2012. Initiation of the western branch of the east African rift coeval with the eastern branch. Nat. Geosci. 5 (4), 289–294.
Rogers, N., 2006. Basaltic magmatism and the geodynamics of the east African rift system. Geological Society, London, Special Publications 259 (1), 77–93.
Rooney, T.O., 2017. The Cenozoic magmatism of east-Africa: Part i–flood basalts and pulsed magmatism. Lithos 286, 264–301.
Rychert, C.A., Hammond, J.O., Harmon, N., Kendall, J.M., Keir, D., Ebinger, C., Bastow, I.D., Ayele, A., Belachew, M., Stuart, G., 2012. Volcanism in the Afar rift sustained by decompression melting with minimal plume influence. Nat. Geosci. 5 (6), 406–409.
Samuel, H., Farnetani, C.G., 2003. Thermochemical convection and helium concentrations in mantle plumes. Earth Planet. Sci. Lett. 207 (1), 39–56.
Seton, M., Müller, R., Zahirovic, S., Gaina, C., Torsvik, T., Shephard, G., Talsma, A., Gurnis, M., Turner, M., Maus, S., Chandler, M., 2012. Global continental and ocean basin reconstructions since 200 Ma. Earth Sci. Rev. 113 (3), 212–270.
Shephard, G.E., Müller, R.D., Seton, M., 2013. The tectonic evolution of the Arctic since Pangea breakup: integrating constraints from surface geology and geophysics with mantle structure. Earth Sci. Rev. 124, 148–183.
Sleep, N.H., 1988. Gradual entrainment of a chemical layer at the base of the mantle by overlying convection. Geophys. J. Int. 95 (3), 437–447.
Stankiewicz, J., de Wit, M.J., 2005. River networks of southern Africa: scaling laws governing their geometry and deviations from scaling. Geochem. Geophys. Geosyst. 6 (9). https://doi.org/10.1029/1999GC000035.
Steinberger, B., 2000. Plumes in a convecting mantle: models and observations for individual hotspots. J. Geophys. Res.: Solid Earth 105 (B5), 11127–11152, 1978–2012.
Steinberger, B., O'Connell, R.J., 1998. Advection of plumes in mantle flow: implications for hotspot motion, mantle viscosity and plume distribution. Geophys. J. Int. 132 (2), 412–434.
Steinberger, B., Torsvik, T.H., 2012. A geodynamic model of plumes from the margins of large low shear velocity provinces. Geochem. Geophys. Geosyst. 13 (1). https://doi.org/10.1029/2011GC003808.
Tackley, P.J., 1998. Three-dimensional Simulations of Mantle Convection with a Thermo-Chemical Basal Boundary Layer: D"? In: Gurnis, M., Wysession, M.E., Kittle, E., Buffett, B.A. (Eds.), The Core-Mantle Boundary Region. Geodynamics Series, pp. 231–253.
Tan, E., Gurnis, M., 2005. Metastable superplumes and mantle compressibility. Geophys. Res. Lett. 32 (20). https://doi.org/10.1029/2005GL024190.
Tan, E., Leng, W., Zhong, S., Gurnis, M., 2011. On the location of plumes and lateral movement of thermochemical structures with high bulk modulus in the 3-d compressible mantle. Geochem. Geophys. Geosyst. 12 (7). https://doi.org/10.1029/2011GC003665.
Underwood, C.J., King, C., Steurbaut, E., 2013. Eocene initiation of nile drainage due to east African uplift. Palaeogeogr. Palaeoclimatol. Palaeoecol. 392, 138–145.
van der Meer, D.G., Spakman, W., van Hinsbergen, D.J., Amaru, M.L., Torsvik, T.H., 2010. Towards absolute plate motions constrained by lower-mantle slab remnants. Nat. Geosci. 3 (1), 36–40.
Van Keken, P., King, S., Schmeling, H., Christensen, U., Neumeister, D., Doin, M.-P., 1997. A comparison of methods for the modeling of thermochemical convection. J. Geophys. Res.: Solid Earth 102 (B10), 22477–22495.
Zhong, S., 2006. Constraints on thermochemical convection of the mantle from plume heat flux, plume excess temperature, and upper mantle temperature. J. Geophys. Res.: Solid Earth 111 (B4), 1978–2012.
Zhong, S., Hager, B.H., 2003. Entrainment of a dense layer by thermal plumes. Geophys. J. Int. 154 (3), 666–676.
Zhong, S., McNamara, A., Tan, E., Moresi, L., Gurnis, M., 2008. A benchmark study on mantle convection in a 3-D spherical shell using Citcoms. Geochem. Geophys. Geosyst. 9 (10). https://doi.org/10.1029/2008GC002048.
Zhong, S., Zuber, M.T., Moresi, L., Gurnis, M., 2000. Role of temperature-dependent viscosity and surface plates in spherical shell models of mantle convection. J. Geophys. Res.: Solid Earth 105 (B5), 11063–11082. https://doi.org/10.1029/2000JB900003.